Materials Science & Engineering A 734 (2018) 491–505

Contents lists available at ScienceDirect

Materials Science & Engineering A

journal homepage: www.elsevier.com/locate/msea

Investigation of short-term creep deformation mechanisms in MarBN steel at elevated temperatures

A. Benaarbia[a,*], X. Xu[b], W. Sun[a], A.A. Becker[a], Mark A.E. Jepson[b]

[a] Department of Mechanical, Materials and Manufacturing Engineering, University of Nottingham, Nottingham, Nottinghamshire NG7 2RD, UK
[b] Department of Materials, Loughborough University, Loughborough, Leicestershire LE11 3TU, UK

ARTICLE INFO

Keywords:
MarBN steel
Dislocation climb
Plastic instability
Short-term creep

ABSTRACT

This paper reports the short-term creep behaviour at elevated temperatures of a MarBN steel variant. Creep tests were performed at three different temperatures (625°C, 650°C and 675°C) with applied stresses ranging from 160 MPa to 300 MPa, and failure times from 1 to 350 h. Analysis of the macroscopic creep data indicates that the steady-state creep exhibits a power-law stress dependence with an exponent of 7 and an activation energy of 307 kJ mol^{-1}, suggesting that dislocation climb is the dominant rate-controlling creep mechanism for MarBN steel. Macroscopic plastic instability has also been observed, highlighted by an obvious necking at the rupture region. All the macroscopic predictions have been combined with microstructural data, inferred from an examination of creep ruptured samples, to build up relations between macroscopic features (necking, damage, etc.), and underlying microstructural mechanisms. Analysis of the rupture surfaces has revealed a ductile fracture mode. Electron Backscatter Diffraction (EBSD) analysis near to the rupture surface has indicated significant distortion and refinement of the original martensitic substructure, which is evidence of long-range plastic flow. Dislocation pile-ups and tangles from TEM were also observed near substructure boundaries and precipitate particles. All of these microstructural observations suggest that creep is influenced by a complex interaction between several elements of the microstructure, such as dislocations, precipitates and structure boundaries. The calculated stress exponent and activation energy have been found to agree quantitatively with the highlighted microstructural features, bearing some relationships to the true observed creep microstructures.

1. Introduction

The 9–12% Cr steels have a combination of good creep properties and sufficient oxidation resistance, with additional benefits from good thermal properties and cost effectiveness [1,2]. The recently developed tempered martensitic MarBN steel (9Cr-3W-3Co-VNbBN) belongs to the family of the 9–12% Cr steel and is expected to be used in ultra-supercritical power plant (USC) [3]. This material contains boron and nitrogen at minor levels in combination with solid solution and precipitation strengthening elements to deliver improved microstructural stability that is beneficial for long-term creep performance.

Following Andrade [4], three stages can be considered in a typical creep curve: the reduced stage, the steady-state stage and the accelerated stage. Studying these three stages helps in understanding the whole creep process. Creep occurs as a result of interaction (or competition) of both the work hardening process caused by the applied force (experienced as a decrease of the strain rate) and annealing process due to elevated temperature [5], resulting in strong microstructural changes (grain boundary sliding, dislocation climb, etc.) [6,7]. These microstructural changes can significantly affect the mechanical features of the material. As the creep deformation begins to increase (reduced stage), the number of dislocations in the material increases and the material becomes harder to deform. Dislocations can thus climb and re-arrange themselves (recovery process). This results in a dynamic equilibrium between the new dislocations caused by plastic deformation and cancellation in the recovery process. Thus, the creep rate becomes almost constant (steady state) and local stress concentrations at grain boundaries causes nucleation of cavities and pores [5]. Most of the creep life is spent in the steady stage with its duration being material-dependent. When these microstructural changes develop into large-scale structural damage, the material fails due to formation of micro-cracks within grains and cavitation at grain boundaries (accelerated stage).

The steady-state creep rate often shows a power law dependence on the applied stress, σ, and an Arrhenius type law dependence on the temperature, T. A number of creep-related material properties can be

* Corresponding author.
E-mail address: adil.benaarbia@nottingham.ac.uk (A. Benaarbia).

https://doi.org/10.1016/j.msea.2018.06.063
Received 25 May 2018; Received in revised form 14 June 2018; Accepted 15 June 2018
Available online 18 June 2018

deduced from the steady-state data. The steady-state creep, rate (SSCR), the stress exponent, n*, the activation energy for creep, Q*, and the mean creep rate, (ϵ_f/τ_f), where ϵ_f and τ_f, the fracture strain and rupture time respectively, are the most important creep features. These properties can be determined, when a threshold stress σ_o, is considered, by simple prominent phenomenological laws known as the Park et al. [8] and the modified Monkman-Grant (MG) [9] formulae:

$$\begin{aligned} &\text{SSCR} = \varphi E(T)^{-n^*}(\sigma - \sigma_o)^{n^*}\exp(-Q^*/\mathscr{R}T);\\ &\text{SSCR}^{\xi} = \omega\epsilon_f/\tau_f, \end{aligned} \tag{1}$$

where φ is a material function, E is the Young's modulus that depends on temperature, and $\mathscr{R}$ denotes the universal gas constant, while terms ξ and ω stand for the MG constants which are temperature independent. These equations are extensively used in power plant engineering applications to predict both SSCR and τ_f by extrapolation to lower stress levels. The Monkman-Grant relation is no longer valid for materials that exhibit large tertiary creep and limited steady state (a correction in terms of the fracture strain, ϵ_f, and the strain at the onset of tertiary stage, τ_{ss} has to be incorporated [10]). A number of studies have been reported in the literature on extrapolation methods based on creep rupture curves to characterise the change in creep mechanisms [11,12], and development has been made in assigning specific values of both n* and Q* to the underlying microstructural processes [13–16]. Indeed, creep is generally controlled by diffusion at a low stress when the exponent, n*, is close to unity[1] [17]. This behaviour is denoted as "Nabarro-Herring" creep (atoms diffuse through the lattice causing grains to elongate along the stress axis) for higher homologous temperatures and "Coble creep" (atoms diffuse along the grain boundaries resulting in grain elongation in the direction of stress) at lower temperatures. At an intermediate stress level, creep is attributed to dislocation movement ("n*-power-law" regime) for which the exponent n* is typically between 3 and 7 [14]. However, the values of n* exceed 7 at higher stress levels and the behaviour is termed power-law-breakdown or exponential creep [18]. The mechanism of steady-state creep deformation in the power-law-breakdown regime is more complicated and still not completely understood.

The creep properties of the 9% Cr steels are, indeed, linked with microstructural characteristics. The initial microstructure of these steels is typically composed of a tempered martensitic matrix in combination with secondary precipitate phases including grain boundary $M_{23}C_6$ carbides and intragranular MX carbonitrides [19]. A high dislocation density in the matrix, as commonly observed in martensitic steels, provides a structural strengthening effect that contributes to good mechanical properties and creep resistance, whereas secondary precipitate phases deliver additional precipitation strengthening by stabilising lath and grain boundaries and hindering dislocation movement [20]. Upon creep exposure, the degradation of the martensitic matrix is typically identified by a decrease in dislocation density and the coarsening of the substructure, accompanied with extensive dislocation interactions such as dislocation tangles and dislocation jogs [21–26]. The formation of sub-grains within the martensitic laths also occurs during creep via the formation of dislocation networks within the lath interiors, leading to a decrease in dislocation density upon further growth of sub-grains during creep [24]. Both the coarsening of pre-existing laths and the formation of sub-grains are accelerated under increased temperature and stress levels, with the latter being more influential on the rate of microstructural degradation [20,24].

The coarsening of the pre-existing secondary precipitates during creep was also extensively reported in previous studies of 9% Cr steels [27–30]. This was linked with the deterioration of creep resistance, particularly under long-term creep testing conditions, due to a loss of particle pinning effects to stabilise the martensitic microstructure [19,27,31]. Although not as significant as for long-term creep exposure, the coarsening of secondary precipitates was also observed in 9% Cr steels after short-term creep and was considered as a possible microstructural factor contributing to the deterioration of creep resistance [27,32].

Fractography and damage assessments have also been conducted to investigate the formation of damage in 9% Cr steels after short-term creep testing. Fractography has revealed a typical ductile fracture surface consisting of dimples formed by transgranular fracture [26,32,33]. The association of dimples and creep cavities with inclusion particles was also reported in previous studies [26,33], suggesting that creep damage is preferentially nucleated on inclusion particles. Detailed observation from the cross-section after short-term creep tests also revealed the presence of elongated micro-voids and micro-cracks [26,33] that are similar to plasticity induced damage formed at a high strain rate [7].

Most of the existing studies on 9% Cr steels have been conducted in the medium to the long term creep regimes, whereas limited studies [26,33] have been conducted on short duration creep to understand the related creep mechanisms. The research work presented here was mainly carried out at high stress conditions and elevated temperatures, and aims to developing an insight into the rate-controlling creep deformation processes in MarBN steel. The relationship that may exist between the macroscopic behaviour (in terms of creep deformation parameters, such as stress exponent, activation energy and cross-section reduction) and the underlying microscopic mechanisms (dislocation interaction, coarsening of precipitates and lath structure, damage characteristics, etc.) has been investigated. Another objective consists of decoupling both creep and local plasticity instability observed in failed MarBN specimens. The elucidation of these global and local creep mechanisms will facilitate the identification of the operating creep mechanisms in the MarBN steel, and thus contribute to the understanding of the creep rupture behaviour after short-term creep exposure.

2. Material and experimental methods

The experimental investigation was conducted on a recently developed creep-resistant MarBN steel. The chemical composition of the steel is given in Table 1. Cylindrical uniaxial specimens with a 50 mm gauge length and a 10 mm gauge diameter (see Fig. 1) were machined from forged bars. Before manufacturing the samples, the as-forged bars were normalised at 1200°C for 4 h and tempered at 765°C for 3 h, to obtain a coarse-grained tempered martensitic microstructure, Fig. 2.

Short-term creep tests were carried out using a creep testing machine equipped with a resistance heating furnace with a maximum operating temperature of 800°C. Three thermocouples were mounted on the specimen inside the furnace to control and track the furnace temperature. The tests were performed at different stress levels ranging from 160 MPa to 300 MPa and three temperatures: 625°C, 650°C and 675°C. The values of the applied stress were chosen such that the test durations were less than 350 h (thus equivalent to a stress range close to, but less than, the yield stress) to emphasize the effect of local plasticity on the rupture behaviour of the MarBN steel. After short-term

Table 1
Chemical composition of the investigated material (all elements are in wt%, B and N are in ppm).

C	Si	Mn	P	S	Cr	Mo	Ni
0.1	0.45	0.54	0.012	0.004	8.74	0.05	0.14
Al	**B**	**Co**	**Cu**	**Nb**	**V**	**W**	**N**
0.007	120	3.02	0.04	0.06	0.21	2.53	180

[1] Although fundamental creep deformation theory suggests a value of one in the diffusion creep regime, there are some reports of higher values up to about 3 (for example see. [66]).

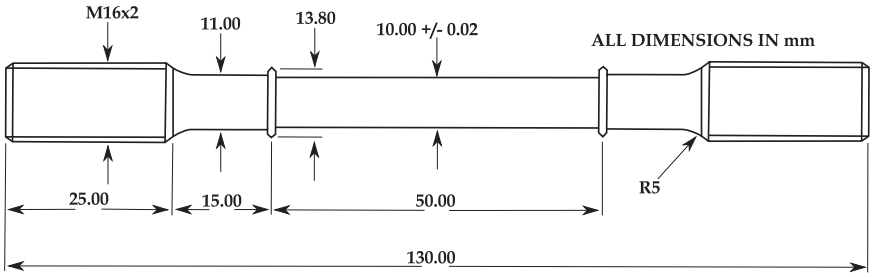

Fig. 1. Uniaxial creep test samples used for the experimental work.

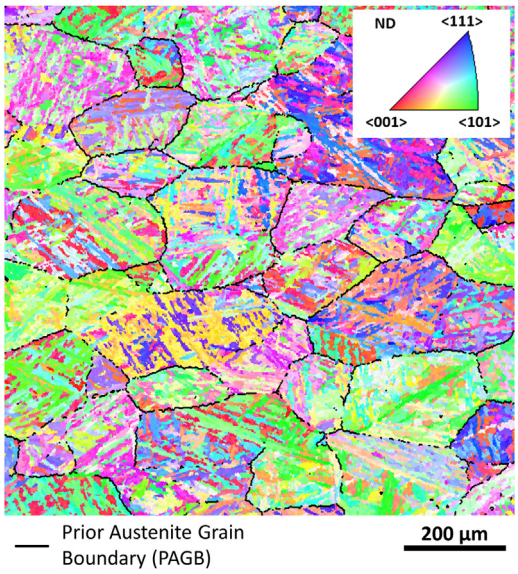

Fig. 2. An EBSD orientation map providing an overview of the microstructure of the as-received material. The partition of boundaries with a misorientation range of 20° – 50° is shown in black to highlight the Prior Austenite Grain Boundaries (PAGBs).

creep tests, creep ruptured specimens were sectioned along the centre line of the gauge portions to facilitate detailed microstructural characterisation of the cross-sections. The samples were prepared using conventional metallographic preparation procedures, which involved an initial grinding stage on SiC with water, polishing stages using 6 µm and 1 µm diamond suspensions and a final chemo-mechanical polishing stage using a suspension of 0.06 µm colloidal silica.

Fractography of the rupture surfaces was conducted using a Leo 1530VP Field Emission Gun (FEG) Scanning Electron Microscope (SEM) with Secondary Electron (SE) micrographs collected using an In-lens annular detector. Back Scattered Electron (BSE) micrographs were collected using a JEOL® JSM-7800F FEG-SEM to study the distribution of damage and inclusions in the as-received material, gauge and head portions of the ruptured specimens. In the as-received material and the head portions, 25 BSE micrographs covering a total area of ~300,000 µm^2 were collected from each location. BSE micrographs were also collected along the centre of each specimen at intervals of 0.5 mm to determine the variation of damage within the gauge portions. The characteristics of the martensitic microstructure were investigated using Electron Backscatter Diffraction (EBSD) in an FEI® Nova Nanolab 600 dual-beam Focused Ion Beam (FIB)/FEG-SEM equipped with an EDAX® Hikari EBSD camera. In the as-received material and the head portions, five EBSD maps measuring 50 µm × 50 µm were collected to quantitatively analyse the grain structure with sufficient statistical significance. Three EBSD maps of the same size were also collected from the gauge portions of the specimens that were tested at 650°C to investigate the grain structures in the regions 0.1 mm, 5.0 mm and 20.0 mm from the rupture surface. The area of individual martensitic blocks and the length density of martensitic boundaries were quantitatively measured from the EBSD maps. The elongation of the martensitic microstructure along the principal stress direction was also determined using the line intercept method with the direction of lines in parallel with the nominal stress direction. The intercept length of the grains in the gauge portion was normalised for comparison with the head portion using the following equation:

$$\ell_{nor} = \ell_{meas}(\Lambda_{head}/\Lambda_{gauge})^{1/2}, \quad (2)$$

where ℓ_{nor}, ℓ_{meas}, Λ_{head} and Λ_{gauge} are the normalised intercept length, the experimentally measured intercept length, the average area of the grains in the head and the gauge portions, respectively. The distribution characteristics of secondary precipitates were quantitatively analysed using ion beam induced SE imaging enhanced using in-situ XeF_2 gas etching in the dual beam FIB/FEG-SEM with a Ga^+ ion source operated at an accelerating voltage of 30 kV. From each specimen, 10 micrographs covering a total area of ~1500 µm^2 were collected at random areas with a minimum spacing of 500 µm. The number density and the average size of secondary precipitates were measured from the obtained micrographs using a grey scale segmentation method. Thin-foil specimens were prepared using a FIB-based lift-out technique [34] in the dual beam FIB/FEG-SEM with specimen surfaces at approximately 45° to the principal stress direction. The thinning process was conducted using the Ga^+ ion source operated at an accelerating voltage of 30 kV with a minimum ion beam current of 0.1 nA. A final cleaning process was also performed on the electron-transparent region at a lower accelerating voltage of 5 kV. An FEI® Tecnai® F20 Transmission Electron Microscope (TEM) was used for diffraction contrast imaging of dislocations in the Bright Field Scanning Transmission Electron Microscopy (BF-STEM) mode with an electron beam direction close to the < 001 > zone axis [35,36]. The chemical composition of precipitates was also analysed using Energy Dispersive X-ray spectroscopy (EDX) with an Oxford Instruments X-Max 80^N TLE EDX system in the same TEM system at an accelerating voltage of 200 kV.

3. Results

3.1. Creep behaviour analysis

The short-term creep curves that were obtained under different temperatures and stresses are presented in Fig. 3 with corresponding creep properties in Table 2. All data extracted from the creep curves exhibit the following main characteristics: *i)* the steady-state is of long duration and, in most cases, does not exceed 3% strain, *ii)* the accumulation of strain in the tertiary stage (ε_f) is much higher compared to that in both reduced (ε_{st}) and steady-state (ε_{ss}) creep regimes, and *iii)* significant necking is observed during the final stage of creep (see Fig. 4). All these observations suggest that the dramatic increase in strain observed in the tertiary stage is a result of macroscopic plastic instability prior to the fracture (a loss of balance between the increase in strength due to hardening and increase in stress due to the reduction in cross-section area (RA)). The specimen fractured when the reduction

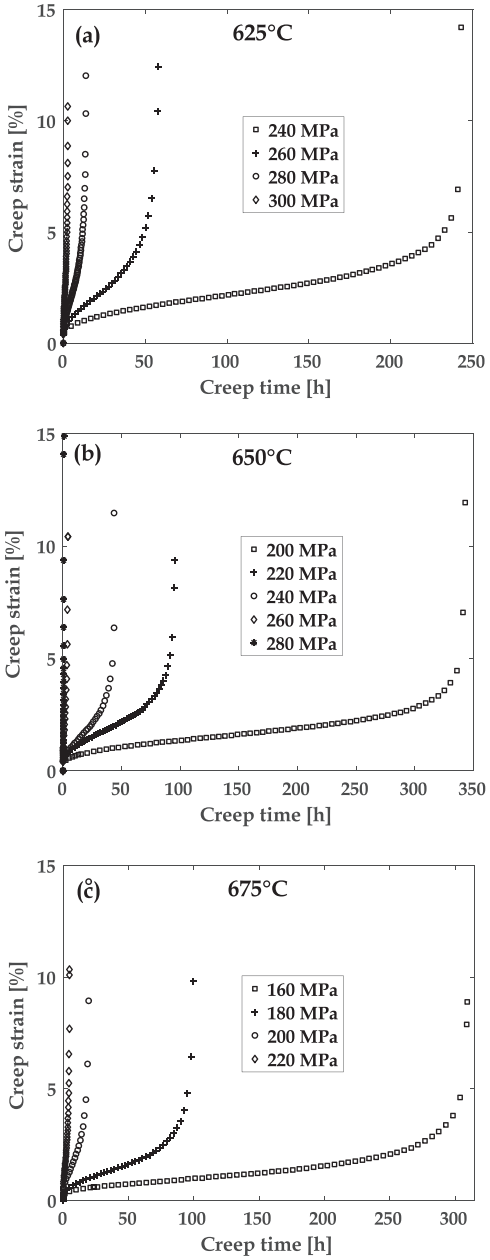

Fig. 3. Strain-time curves for creep tests conducted on MarBN samples at the selected temperatures: (a) 625°C, (b) 650°C, (c) 675°C.

in cross-section reached 59–83% depending on the temperature and applied stress levels.

A number of creep material properties can be deduced from the uniaxial creep curves, including the value of the steady-state creep rate (SSCR), the time to fracture (τ_f) and the mean creep rate (ε_f/τ_f). The interaction between all of these creep properties is shown in Fig. 5. For all the selected temperatures, the creep properties can be comprehensively expressed using the following expressions (simple power-law and modified Monkman-Grant relationships):

$$\tau_f = \mathrm{p}(T)\sigma^{-\mathrm{m}(T)};\ \mathrm{SSCR} = \mathrm{q}(T)\sigma^{\mathrm{n}(T)};\ \mathrm{SSCR}^{\xi} = \omega\varepsilon_f/t_f, \tag{3}$$

where p(T), q(T), m(T) and n(T) are temperature-dependent creep functions while ξ and ω stand for the Monkman-Grant (MG) constants which are found to be temperature independent. The apparent values of the creep properties defining rupture life-stress (respectively SSCR)

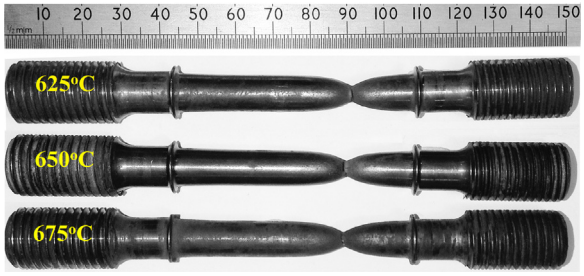

Fig. 4. MarBN specimens after creep testing showing necking.

relationships at the selected temperatures and applied stresses are given in Table 3. The computed values of apparent stress exponents n and m are very high due to the high stresses employed.[2] Good correlation with the modified Monkman-Grant (MG) relationship was also observed for the rupture creep-life data (Fig. 5c). With the increase of SSCR, the mean creep rate (ε_f/τ_f) increases in a roughly straight line slope of 0.88. It is worth noting that such approach is widely used in high-temperature engineering to determine the creep life of structural components. Developing predictive models to estimate rupture time of MarBN from the results of short term tests is of particular interest. The Monkman-Grant relationship has been shown to be valid for most metals and alloys used in creep resistant applications [37]. However, such an approach cannot be valid for long-term behaviour since the prediction of longer term creep properties from short term creep data may be inaccurate causing overestimation of long term creep rupture time [38].

The creep strain accumulation is also a thermally-activated process. According to the creep data presented beforehand, the functional dependence of the steady-state rates on temperature follows an Arrhenius-type law where the apparent activation energy for creep, Q(σ), is a stress-dependent function. Values of the apparent activation energy at the selected stress levels are also compiled in Table 3 (these values decrease with increasing applied stress). It can be seen that these values are much higher and do not reflect the true value of the activation energy. Higher apparent creep activation energies for different high strength Cr-Mo steels have also been reported by different studies [39,40].

As mentioned previously, both the values of apparent stress exponent, n and apparent activation energy, Q, obtained beforehand, are high and cannot reflect the true rate-controlling creep mechanism. This is because they were computed for a constant substructure model by assuming that the microstructure remains constant during creep and subsequent failure, which is not entirely true for the MarBN steel where substantial microstructural evolution is observed during creep exposure (e.g. dynamic precipitate distribution, dislocation structure and lath/grain structure). Some researchers have pointed out that the true values of the stress exponent, n*, and activation energy, Q*, can be assessed by considering the variation of Young's modulus with temperature and by introducing the concept of creep threshold stress [41]. The stress threshold, denoted hereafter by σ_o, is introduced to explain variations of the stress exponent and activation energy with the applied stress. Using Eq. (1b), the effective stress (i.e. $\sigma_{eff} = \sigma - \sigma_o$) can be determined following the equation given below:

$$\sigma_{eff} = \phi\mathrm{SSCR}^{1/\mathrm{n}^*},\ \phi = E\varphi^{-1/\mathrm{n}^*}\exp(\mathrm{Q}^*/\mathrm{n}^*\mathscr{R}T). \tag{4}$$

Several values of stress exponent, n* were considered to emphasize whether the rate-controlling creep mechanism is viscous glide[3] (n* =

[2] To rationalise the high apparent stress exponents, a threshold stress, defined as the stress below which no creep deformation occurs [67], is often considered to elucidate the true creep mechanisms.

[3] Viscous glide creep is generally characterized by the absence of subgrains [18].

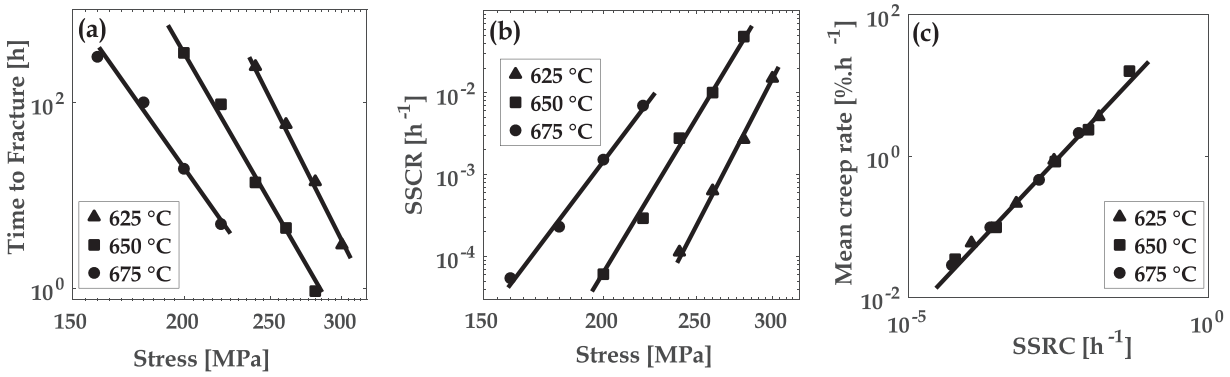

Fig. 5. (a) Time to fracture as a function of applied stress. (b) SSCR versus applied stress. (c) Mean creep rate (ε_f/τ_f) versus SSCR plotted according to the modified Monkman-Grant relation-ship (see. Eq. (3)).

Table 2
Material creep features associated with the uniaxial creep curves plotted in Fig. 3. τ_{st} denotes the transient creep time.

T [°C]	σ [MPa]	ε_{st} [%]	τ_{st} [h]	ε_{ss} [%]	τ_{ss} [h]	SSCR [$10^{-4}\times$ h^{-1}]	τ_f [h]	ε_f [%]	RA [%]
625	240	1.42	33.54	2.97	168.51	1.14	242.88	14.21	60.31
	260	1.43	8.68	2.87	32.15	6.34	58.04	12.43	70.84
	280	1.43	1.73	2.54	6.71	27.03	13.93	12.02	79.75
	300	1.44	0.52	2.79	1.44	149.01	2.93	10.65	82.02
650	200	1.04	46.84	2.18	243.41	0.61	342.91	11.93	62.05
	220	1.09	11.33	2.63	66.71	2.91	95.47	9.36	73.68
	240	0.82	3.73	2.26	10.05	28.03	13.73	11.48	74.29
	260	0.78	0.21	2.31	2.01	100.02	4.43	10.43	75.11
	280	0.78	0.08	2.79	0.51	485.12	0.94	14.88	81.08
675	160	0.55	18.07	1.44	185.01	0.54	309.53	8.89	59.04
	180	0.71	8.61	1.91	61.68	2.33	99.82	9.82	72.96
	200	0.81	0.99	2.26	11.03	15.13	19.36	8.93	77.62
	220	0.83	0.35	2.26	2.49	69.27	4.88	10.33	81.42

Table 3
Apparent values of creep function coefficients for MarBN steel. The values of MG constants are found independent of temperature. In the Arrhenius law, ϱ stands for a material constant that depends on temperature. The values of Q are extracted by plotting ln (SSCR) against the reciprocal temperature $1/T$ under the constant stress level and assuming that the apparent stress exponent n is constant over the regime examined.

Applied temperature	T [°C]	**625**	**650**	**675**
Time to fracture $\tau_f = \mathbf{p(T)}\sigma^{-\mathbf{m(T)}}$	p [(MPa)$^{-1}$ h]	2.69×10^{49}	7.59×10^{42}	1.91×10^{31}
	m [-]	19.77	17.53	13.02
Steady-state creep rate SSCR $= \mathbf{q(T)}\sigma^{\mathbf{n(T)}}$	q [(MPa h)$^{-1}$]	1.25×10^{-56}	1.07×10^{-50}	1.17×10^{-38}
	n [-]	21.84	19.88	15.27
Monkman-Grant relationship SSCR$^{\xi} = \omega\varepsilon_f/\tau_f$	ω [-]	0.635	0.631	0.636
	ξ [-]	0.86	0.87	0.89
Applied stress	σ [MPa]	220	240	260
Activation energy	Q [kJ mol^{-1}]	923.07	882.69	760.58
SSCR $= \mathbf{Q(T)}\sigma^{\mathbf{n(T)}}\exp\left(-\frac{\mathbf{Q}}{\mathbf{RT}}\right)$				

3), climb[4] (n* = 4–7) or lattice-diffusion[5] (n* = 8). The threshold stress, σ_o, was estimated by plotting SSCR$^{1/n^*}$ against σ, and linearly extrapolating these creep data to a zero value of the creep rate (the interaction of the extrapolated line with the X-axis gives the threshold stress at a particular temperature). Examination of creep data reveals that both n* = 7 and 8 yield to the best linear fit between SSCR$^{1/n^*}$ and σ (see. Fig. 6a), with a correlation coefficient greater than 0.99 (see Table 4) for the three selected temperatures. The corresponding values of the threshold stress σ_o are gathered in Table 4. The threshold stress is found to be strongly sensitive to the applied temperature (σ_o increases with decreasing temperature). To determine the relationship between the threshold stress and the assumed stress exponent, SSCR was plotted against the normalised effective stress on logarithmic plot in Fig. 6b. All correctional values of the real stress exponent (n_{exp}) are found to be close to the assumed values of 7 and 8 (see. Table 4). According to Eq. (4), the real activation energy for creep can be evaluated as $Q^* = n^*\mathscr{R}\psi$, where ψ is the slope of the natural logarithm of ϕE^{-1} with respect to the reciprocal temperature $1/T$. Given Young's modulus values for the selected temperatures (see Table 4), the real activation energy values are found equal to 307.82 kJ mol^{-1} and 297.56 kJ mol^{-1} for n* = 7 and 8, respectively. These values are largely lower than the apparent activation energies obtained beforehand. They are close to the lattice self-diffusion energy for Cr (~308.6 kJ mol^{-1}) [42]. It can thus be suggested that dislocation climb is the dominant rate-controlling creep

[4] Climb-controlled creep is characterized by the formation of subgrains whose size is inversely proportional to the applied stress [18].

[5] The lattice diffusion-controlled creep requires that the subgrain size remains constant over the entire stress range [68].

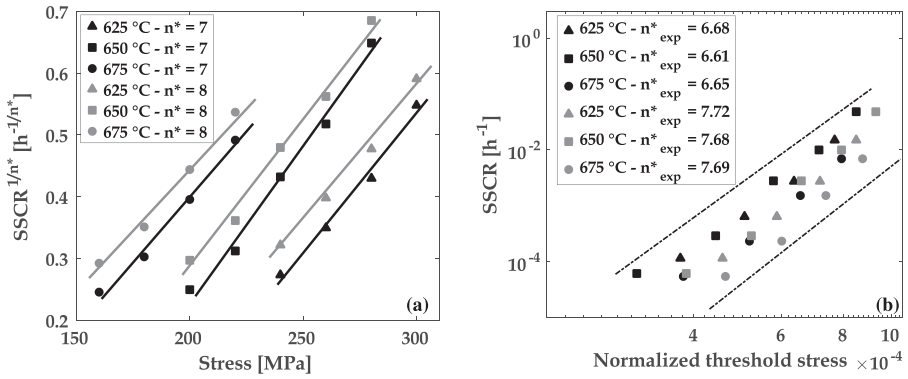

Fig. 6. (a) Minimum creep rate to one-seventh (-eighth) power versus applied stress, (b) Minimum creep rate as function of the normalised effective stress (σ_{eff}/E) for the three selected temperatures.

Table 4
Values of the threshold stress σ_o, the correctional true stress exponent n^*_{exp} and the corresponding correlation coefficient R^2 computed for the selected real stress exponents $n^* = 7$ and 8. Table 4 includes also the values of the corresponding Young's modulus extracted from tensile data conducted on MarBN steel at the selected temperatures.

T [°C]	$n^* = 7$			$n^* = 8$			E [GPa]
	σ_o [MPa]	n^*_{exp}	R^2	σ_o [MPa]	n^*_{exp}	R^2	
625	182.71	6.68	0.994	170.29	7.72	0.996	152.73
650	154.86	6.61	0.992	143.17	7.67	0.994	148.46
675	104.62	6.65	0.992	92.56	7.69	0.993	145.52

mechanism in the MarBN steel. The steady-state creep is therefore exhibiting a power-law stress dependence with an exponent of 7 and a real activation energy of 307.82 kJ mol^{-1}.

By analysing the foregoing results, it is still hard to explore all the deformation mechanisms governing the creep behaviour of the MarBN steel. The power law regime is very flexible and it is feasible to change expressions of the stress exponent and activation energy by adding some internal variables like dislocation density and subgrain size. A fundamental understanding of the microstructural configuration and evolution is therefore needed to emphasize the dominant creep deformation mechanism. All the local changes occurring under creep conditions are of great importance in high-temperature advanced steels because they strongly affect their creep and failure properties. The creep process is naturally accompanied by many different microstructural rearrangements including dislocation movement and grain-boundary cavitation. The emphasis of creep modelling is to combine the macroscopic behaviour and these underlying microscopic mechanisms, in order to build up a direct relation between the strain rate and internal variables such as dislocation density, velocity of climb, internal stress and subgrain size.

3.2. Fractographic examination and damage assessment after short-term creep

The topography of the rupture surfaces and the damage within the cross-sections were characterized using SE imaging. Fig. 7 shows SE micrographs that were collected from the rupture surface and the cross-section of a specimen that was tested at 650°C with an applied stress of 200 MPa.

The rupture surfaces of all the ruptured specimens consist of a shear lip close to the outer rim and a dimpled fracture surface in the central region (Fig. 7a). Similar topography of rupture surfaces have been observed in previous studies of similar material, and was linked with ductile fracture behaviour [26,32,33]. Elongated micro-voids with a size from less than 1 μm to approximately 3 μm were also observed close to the rupture surface from cross-sections (Fig. 7c). In the regions away from the rupture surface, creep induced damage is predominantly in the form of cavities with sizes of less than 1 μm (Fig. 7d).

Micro-voids and cavities that were developed during the short-term creep test were further studied using SE imaging, with the microstructural features associated with micro-voids and cavities identified using EDX (Fig. 8). The association of inclusion particles with micro-voids and cavities was extensively observed in creep ruptured specimens (Fig. 8a). EDX analysis reveals the association of micro-voids in the necked area with both the BN and MnS type inclusions (Fig. 8c–d), whereas the cavities in the regions away from the rupture surface are predominantly associated with the BN inclusion particles (Fig. 8b).

The distribution of damage and inclusions along the longitudinal direction of the gauge portions was also quantitatively assessed from the cross-section of specimens creep tested at 650°C, Fig. 9.

The distribution of inclusions in the head portion (i.e. the hollow circles) is not significantly different from the distribution in the as-received material (i.e. the grey box). However, the average size and the area fraction are higher in all the regions from the gauge portions (i.e. the solid circles) than the head portions (Fig. 9b–c), whereas the number density in the gauge portions is higher only in the regions from the necked part (less than 5 mm from the rupture surface) (Fig. 9a). Since the measurements from BSE micrographs both included the pre-existing inclusion particles and the associated creep induced damage, the distribution characteristics of damage in the gauge portion can be determined from the difference in distribution between the gauge and the head portions. A higher extent of damage was therefore identified in the necked part than in the regions further away from the rupture surface (i.e. > 5 mm) in both of the specimens tested at 200 MPa and 280 MPa. The damage presented in the necked part is higher in number density and lower in average size in the specimen tested at 280 MPa (Fig. 9a–b), whereas the area fraction of damage is similar between both specimens (Fig. 9c). In addition, it was observed that the number density, in the regions that are over 5 mm from the rupture surface, is similar to the number density of inclusions in the as-received material (Fig. 9a). The similar distribution of particles in the region over 5 mm away from the rupture surface to the as-received material indicates that the local damage was preferentially nucleated on inclusion particles, whilst the higher number density in the necked part suggests that the local damage may not be necessarily formed on inclusion particles.

3.3. Microstructural changes during short-term creep

3.3.1. Initial microstructure in the as-received material

The as-received material shows a typical tempered martensitic microstructure in which Prior Austenite Grains (PAGs) are hierarchically divided into packets, blocks and sub-block laths [43]. The PAGs in the as-received material are typically over 100 μm in size with the

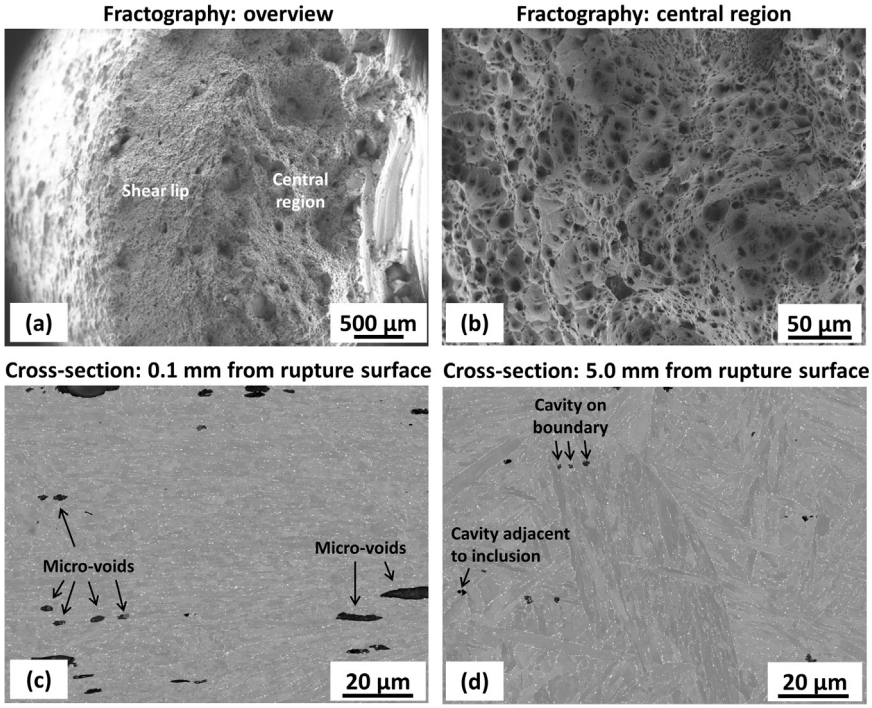

Fig. 7. SE micrographs showing (a and b) the topography of the rupture surface and (c and d) micro-voids or cavities in the cross-section after creep testing at 650°C and 200 MPa.

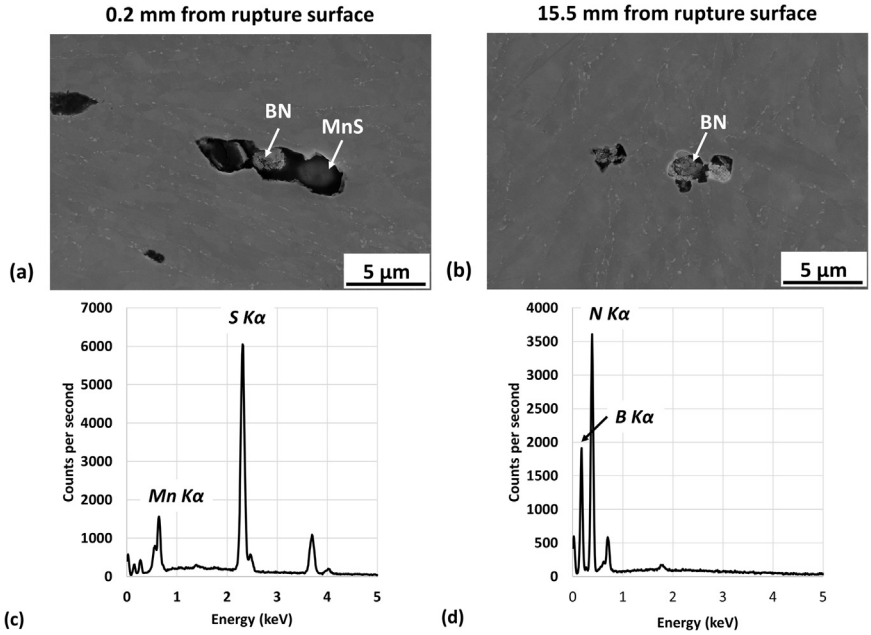

Fig. 8. SE micrographs showing the details of (a) micro-voids near to the rupture surface in the necked area and (b) cavities and inclusions in the regions away from rupture surface after creep testing at 650°C with an applied stress of 200 MPa. The EDX spectra that were collected from (c) MnS and (d) BN inclusions are also included.

misorientation of PAGBs in a range of 20° - 50° (Figs. 2 and 10) [44]. The martensitic blocks are approximately 1.5 µm in width, whereas the misorientation of block boundaries are within a range of 2° - 20° and 50° - 60° due to a Kurdjumov-Sachs orientation relationship with the parental austenitic phases (Fig. 10b) [45]. The size of the martensitic blocks and the length density of martensitic boundaries were quantitatively measured and are presented in Table 5.

The martensitic substructure in the as-received material was further analysed in detail by using STEM. Fig. 11 presents the EDX maps and the high resolution BF-STEM micrographs showing elemental distribution and dislocation structure in sub-block laths, respectively.

The martensitic substructure within an individual block is composed of elongated sub-block laths that are typically a few microns in size and precipitate particles that are distributed both on sub-grain boundaries and within the sub-grain interiors (Fig. 11a). The precipitates that are distributed on sub-grain boundaries are predominantly a few hundred nanometres in size and are relatively more abundant in Cr and W than in the matrix (Fig. 11b–d), which is similar to previously reported observations of $M_{23}C_6$ carbides [46]. The dislocation structure within individual sub-block laths is similar to the existing observations from the tempered martensitic microstructure [36,47], which is a highly-dense dislocation network consisting of straight dislocation lines (Fig. 11e–f). Nano-scale precipitate particles, predominantly less than 5 nm in size were also observed within the laths (Fig. 11e–f). Thorough

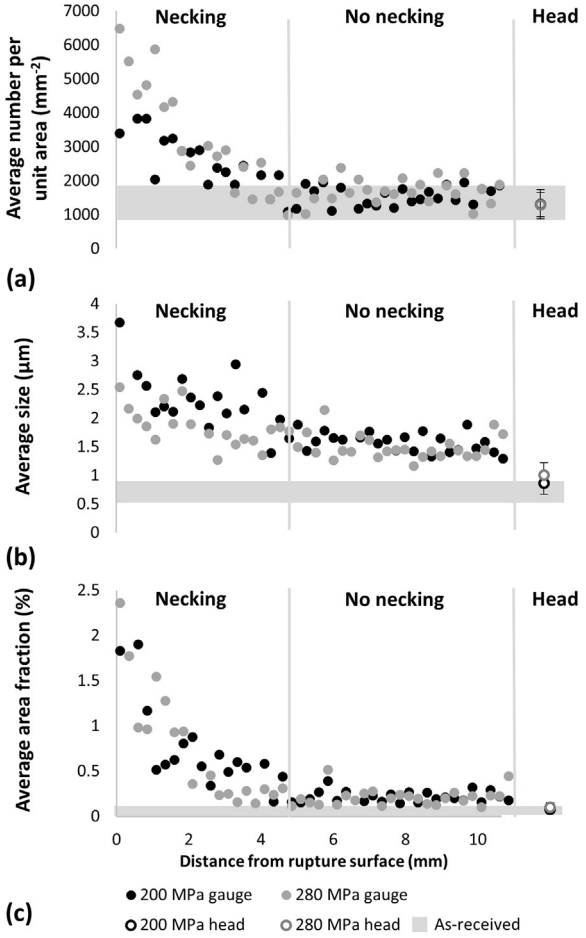

Fig. 9. Graphs showing (a) number per unit area, (b) size and (c) area fraction of creep induced damage and inclusions along the gauge portion of specimens after creep testing at 650°C. The distribution of inclusions in the stress-free head portions and the as-received materials are also included for comparisons.

analysis of the precipitate particles is difficult due to small sizes, but the existing observations from 9% Cr steels suggest that these are fine-scale Nb/V-rich MX carbonitrides [31]. It is worth noting that the MX carbonitrides in MarBN steels are normally smaller in size than the more conventional 9% Cr steels with a higher level of N addition (i.e. 300–700 ppm in Grade 91 and 92 [48]) [19]. MarBN steel is designed to have a lower N level to mitigate the formation of detrimental BN intermetallics as well as to contribute to a well dispersed MX distribution [31].

3.3.2. Microstructural characterisation of creep exposed materials

EBSD maps of samples creep-exposed at 650°C are shown in Fig. 12. After short-term creep testing with an applied stress of 200 MPa, the martensitic microstructure in the region ~20 mm away from the rupture surface (Fig. 12a) is similar to the microstructure in the as-received material (Fig. 10). However, the martensitic microstructure in the specimen tested at 280 MPa is more refined, consisting of blocks with a similar width to the as-received material and smaller grains that are typically 2–3 μm in size (Fig. 12b). In the necked part close to the rupture surface, the pre-existing martensitic microstructure was significantly distorted along the principal stress direction (Fig. 12c–d) at both applied stress levels, accompanied with the formation of a finer martensitic substructure within individual blocks (Fig. 12k–l) in the region 0.1 mm away from the rupture surface. The micro-voids in the regions close to the rupture surface are also elongated in parallel with the principal stress direction (Fig. 12c–d). A higher extent of grain structure distortion and refinement was observed in the specimen tested at a higher applied stress of 280 MPa.

The size of the martensitic blocks and the length of boundaries per unit area were quantitatively measured from EBSD maps. Fig. 13 compares the block size and boundary length densities between the necked gauge regions, non-necked gauge regions and the head portion after creep testing at 650°C.

In both specimens tested at 650°C, the average area and the average intercept length in the head portions are slightly higher than the as-received material (Fig. 13a and c), whereas the length density of the martensitic boundaries from the same regions is slightly lower (Fig. 13b). The characteristics of the martensitic microstructure vary as a function of distance from the rupture surface in the gauge portion. The average area increases, whereas the length density of boundaries decreases as distance from the rupture is increased (Fig. 13a–b). Compared to the specimen tested under 200 MPa, the 650°C/280 MPa specimen shows a lower average area in the regions that are 0.1 mm from the rupture surface (Fig. 13a). This is consistent with previous observations from the martensitic steels in which the substructure becomes more refined at an higher applied stress in the dislocation-climb-controlled creep regime [22,49,50].

The distortion of the original martensitic microstructure under the effect of plastic strain can be better identified by normalising the intercept length along the principal stress direction using the average area in the head portions (Eq. (2)). Compared to the head portion, the

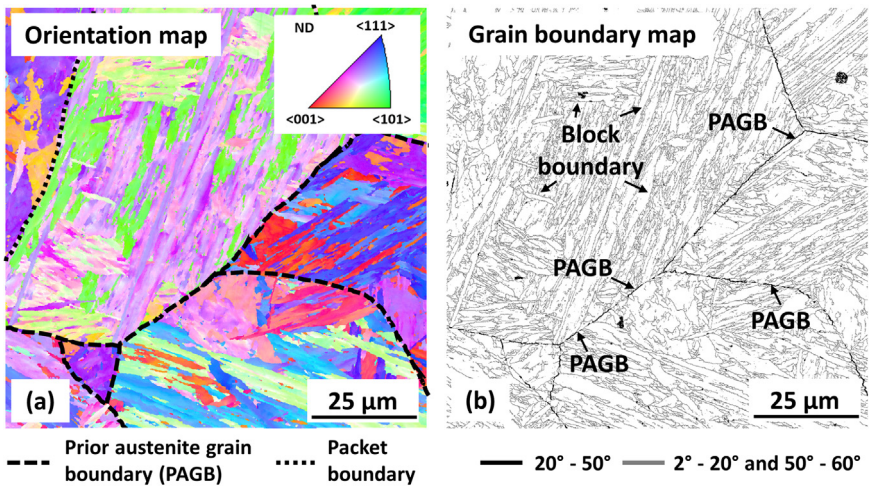

Fig. 10. (a) EBSD orientation and (b) EBSD grain boundary maps showing the characteristics of grain structure and the distribution of grain orientation in the as-received material.

Table 5
The average size of martensitic blocks and the average length density of martensitic boundaries in the as-received material, in which 5 EBSD maps covering an area of ~12,500 μm^2 were collected. The martensitic blocks were defined using a misorientation tolerance of 2°.

Average area of blocks [μm^2]	Block size in intercept length [μm]	Boundary length per unit area [mm/mm^{-2}]
79.9 ± 33.3	1.7 ± 0.5	$1.9 \times 10^3 \pm 1.7 \times 10^2$

normalised intercept lengths are higher in the regions at 0.1 mm and 20 mm away from the rupture surface in the specimens tested under an applied stress of 280 MPa, whereas this characteristic is only higher in the region at 0.1 mm away from the rupture surface in the specimen tested under 200 MPa (Fig. 13d). This indicates that the original microstructure in the regions 20 mm away from the rupture surface was also distorted along the principal stress direction in the specimen tested under an applied stress of 280 MPa, whereas the distortion of the original microstructure only occurred in the region close to the rupture surface in the specimen tested at 200 MPa. This further suggests that plastic deformation was preferentially accumulated in the necked area close to the rupture surface in the specimen tested at 200 MPa, whereas plastic deformation also occurred in the region further away from the

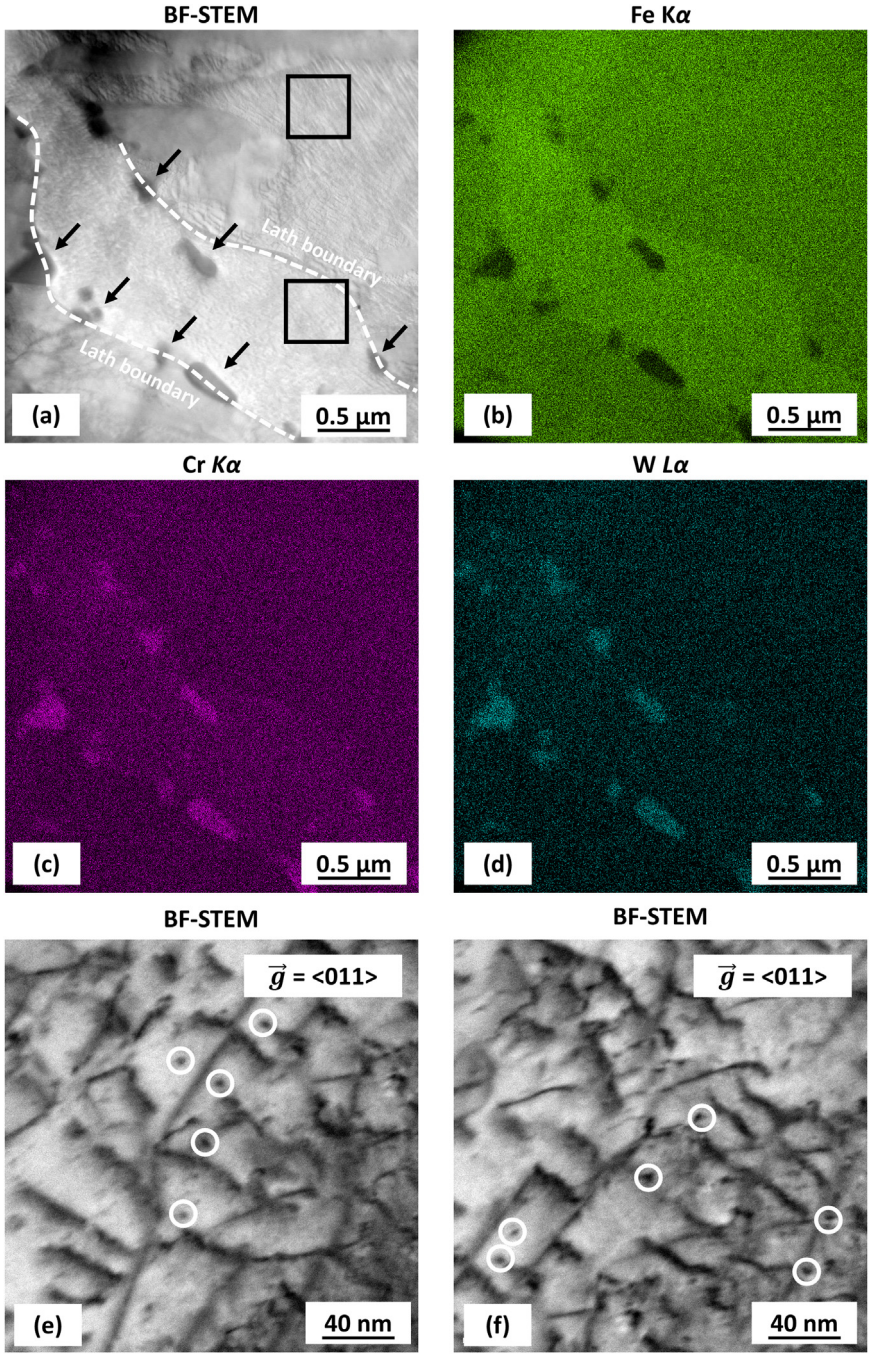

Fig. 11. (a) BF-STEM and (b–d) EDX maps showing the distribution of elements within an individual martensitic lath. The precipitate phase particles that are enriched in Cr and W are indicated by arrows in (a). (e and f) BF-STEM micrographs showing the detailed dislocation structure from the regions as indicated by the black boxes in (a). The nano-scale precipitates presented in the same regions are indicated by white circles in (e and f).

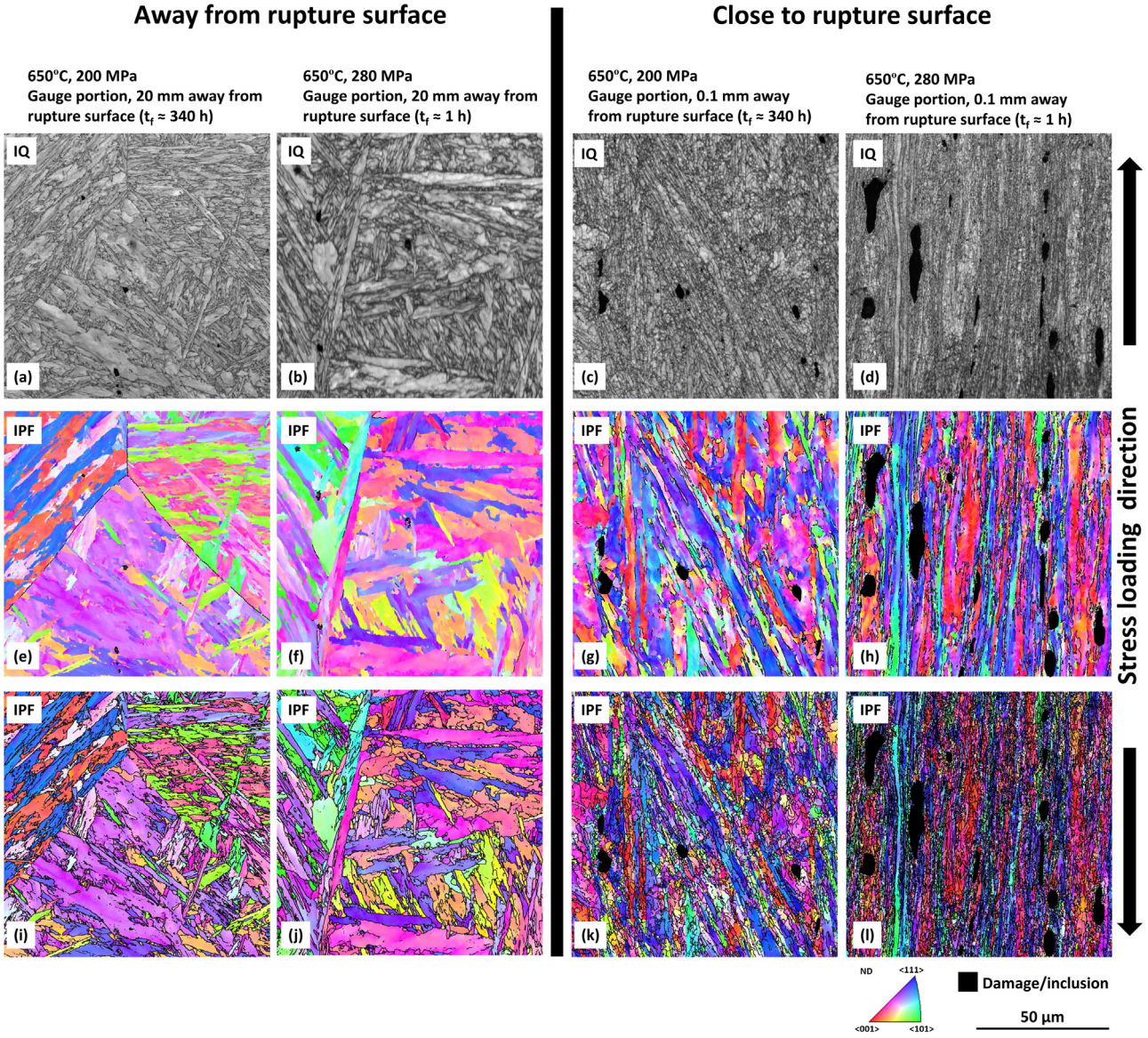

Fig. 12. (a–d) EBSD-IQ and (e-l) EBSD-IPF showing the characteristics of grain structure and distribution of grain orientation after creep testing at 650 °C. The boundaries with a misorientation of 20°- 50° and 2° - 20°/50° - 60° are outlined in (e–h) and (i–l), respectively.

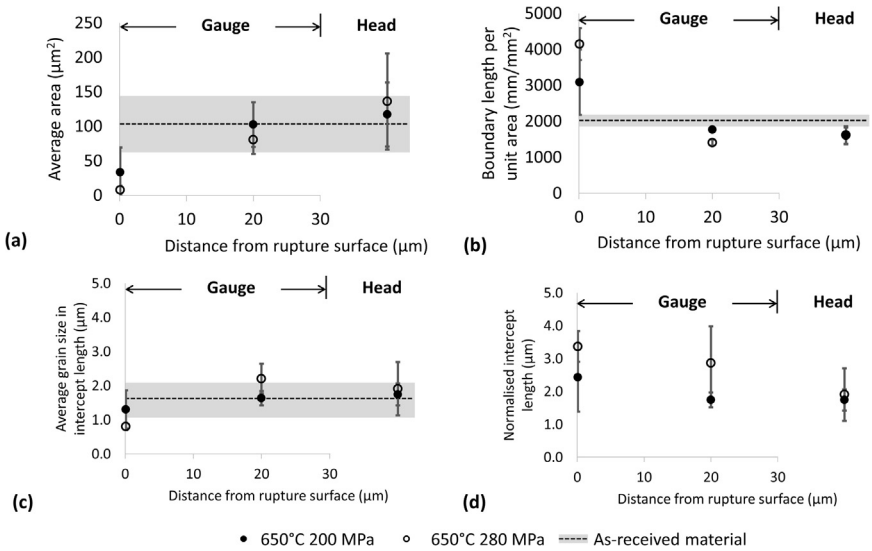

Fig. 13. Graphs comparing (a) average area of martensitic blocks, (b) length density of boundaries, (c) average intercept length and (d) normalised intercept length in the regions that are 0.1 mm and 20.0 mm away from the rupture surface and in the head portion. The data from the as-received material are also included in (a–c) for comparison (grey bar). The standard deviations between the measurements from the same distance from the rupture surface are indicated by half of the lengths of error bars.

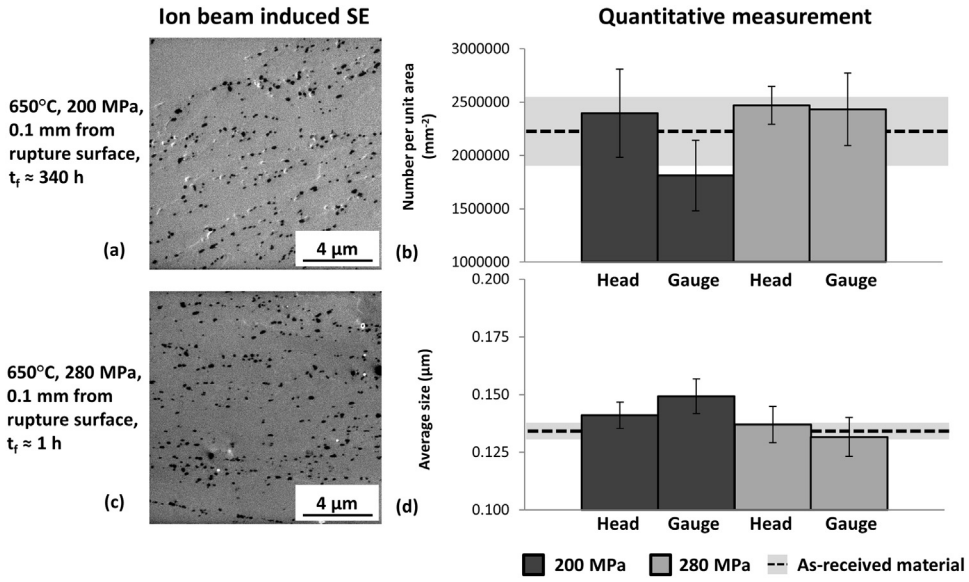

Fig. 14. (a and c) Ion beam induced SE micrographs showing the grain boundary $M_{23}C_6$ carbides in the regions at 0.1 mm from the rupture surface after creep testing at 650 °C. (b and d) Graphs comparing the distribution of precipitate particles between the regions at 0.1 mm from the rupture surface (gauge), the stress-free head portions (head) and as-received material.

rupture surface in the specimen tested at 280 MPa. The average values of the normalised intercept length are also higher in the 650°C/280 MPa specimen compared to the 650°C/200 MPa specimen (Fig. 13d). This observation suggests a higher extent of plastic instability for the specimen tested under an applied stress of 280 MPa, which is also in agreement with the macroscopic observation of a higher reduction of area for the specimen tested at 280 MPa than at 200 MPa (Table 2).

The distribution of Cr and W-rich $M_{23}C_6$ carbides were also investigated using ion beam induced SE imaging. Fig. 14 shows ion beam induced SE micrographs that were collected after creep testing at 650°C and the graphs comparing the distribution of carbide precipitate particles between the regions that are at 0.1 mm from the rupture surface and from the stress-free head portions.

In previous studies of 9% Cr steels, the use of ion beam induced SE imaging has been used successful in the quantitative analysis of $M_{23}C_6$ carbides [51–53]. In the 9% Cr MarBN steel being analysed in this study, this technique was again capable of differentiating the relatively larger $M_{23}C_6$ carbides (Fig. 13a) as dark particles from a relatively brighter background of the matrix (Fig. 14a and c). As shown, there are minor differences between the as-received material and the stress-free head portions for both of the specimens tested at 650 °C. In the specimen tested at an applied stress of 200 MPa, the average value of the number of $M_{23}C_6$ particles per unit area is slightly lower for the region at 0.1 mm from the rupture surface, whereas the average size in the same region is slightly higher than the stress-free head portion (Fig. 14b and d). This indicates that the pre-existing $M_{23}C_6$ carbide particles are slightly coarsened during short-term creep testing at an applied stress of 200 MPa, whereas the carbides in the specimen tested at 280 MPa were not significantly changed due to the short test time period (i.e. ~1 h). The coarsening of carbide particles is detrimental to creep resistance as this deteriorates microstructural stability by losing the pinning effect of substructure boundaries and dislocations [27,32].

The characteristics of the martensitic substructure and dislocation structure in the specimens that were tested at 650°C/200 MPa and 650°C/280 MPa were also studied using BF-S/TEM imaging as shown in Fig. 15.

In the specimen that was tested at 650°C with an applied stress of 200 MPa (Fig. 15a), the sub-block laths are predominantly 1–2 µm in length, whereas a more refined martensitic substructure consisting of sub-block laths of less than 1 µm in length was observed in the specimen tested at an applied stress of 280 MPa (Fig. 15b). In the specimen tested at an applied stress of 200 MPa, some of the laths exhibited a dislocation network consisting of straight dislocation lines (Fig. 15c), similar to the dislocation structure in the as-received material (Fig. 11e-f), whereas a much lower number of dislocations was observed within other sub-block laths in the same specimen (Fig. 15e). Extensive dislocation interactions in the form of dislocation jogs and the interaction of dislocations with nano-scale precipitate particles were also observed in the same laths showing a lower number of dislocations (Fig. 15g). Dislocation pile-ups were also observed close to the relatively larger precipitates on lath boundaries (Fig. 15e). In the specimen tested at an applied stress of 280 MPa, the number of the dislocations within sub-block laths was lower than the as-received material (Figs. 15d and 15f). Dislocation jogs, tangles and pile-ups were also extensively observed within individual laths from the same specimen (Fig. 15d-h). The nano-scale precipitates (MX) in the creep-exposed specimens (Fig. 15g and h) are similar in size to those in the as-received material without creep exposure (Fig. 11). This indicates that the MX carbonitrides were not significantly changed in size during short-term creep, which is consistent with existing observations of MX carbonitrides being more resistant to coarsening than $M_{23}C_6$ during creep exposure [19,54]. The stable MX precipitates enhance the creep resistance of the MarBN steel by improving the stability of the dislocation structure [31,55]. These observations indicate that the microstructure of the MarBN steel is stabilised via structural strengthening and precipitation strengthening mechanisms [19,30,56] to deliver satisfactory creep resistance for industrial applications.

4. Discussion

Experiments have been conducted on MarBN steel over a range of applied stresses and temperatures to 1) build up a direct relationship between the creep strain rate and internal variables, 2) decouple both creep and local plasticity-driven mechanisms, and 3) elucidate the true rate-controlling creep deformation mechanism. The main results are summarised as follows: i) the steady-state creep rate exhibits a power-law stress dependence with an exponent of 7 (SSCR $\propto\sigma^7$), ii) the corresponding real activation energy has been determined to be 307 kJ mol^{-1}, which is close to the lattice self-diffusion energy in Cr (308.6 kJ mol^{-1}) [42], and iii) a macroscopic plastic instability was observed, highlighted by an obvious necking within the gauge length towards the rupture surface.

The dominant creep deformation mechanism for MarBN can be inferred from the n* and Q* values. Following i) and ii), it has been suggested that dislocation climb is the rate-controlling mechanism of

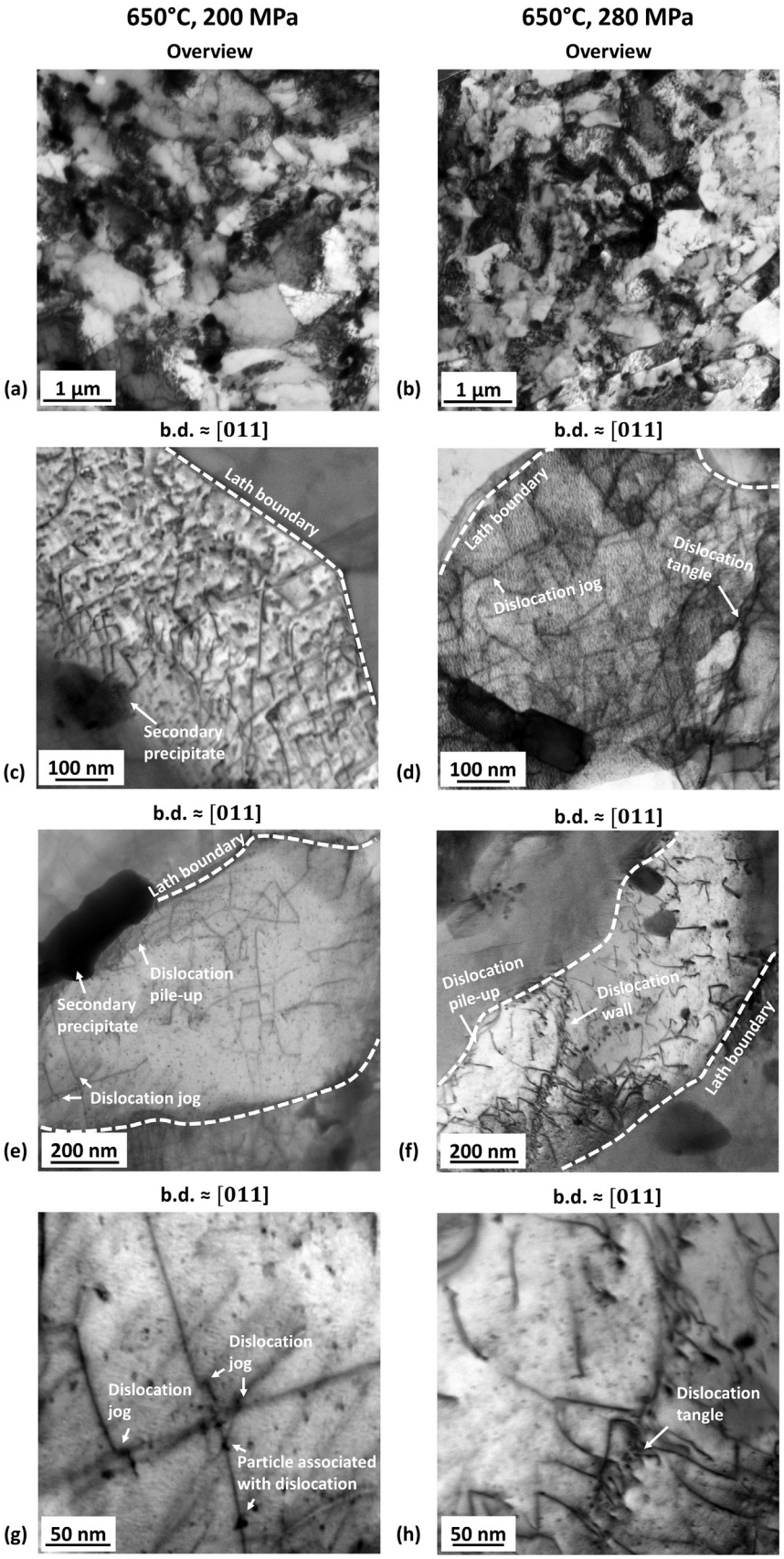

Fig. 15. (a and b) BF-TEM and representative (c-h) BF-STEM micrographs showing the characteristics of the martensitic substructure and dislocation structure within individual sub-grains in the regions 0.5 mm from the rupture surface after creep testing at 650 °C with an applied stress of (a, c, e and g) 200 MPa and (b, d, f and h) 280 MPa.

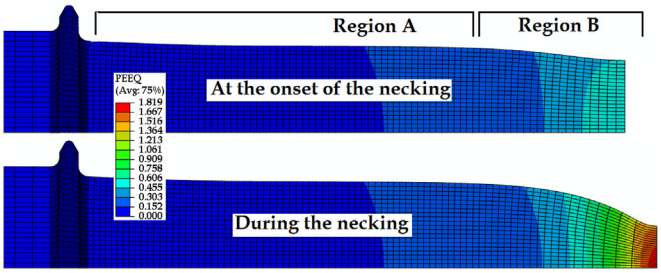

Fig. 16. FE analysis conducted on a MarBN steel specimen using a Benchmark necked-based model showing the spatial distribution, at the onset and during the necking, of the equivalent plastic strain.

creep at both high stress and elevated temperature. Based on the existing studies of creep in polycrystalline metallic materials [18,57] and the more recent studies on other 9% Cr steels [33,58,59], dislocation climb is stated as an out-of-plane movement for edge dislocations. Its rate depends on many factors, including chemical forces, the mobility of jogs and the rate of migration of vacancies [60]. The operation of dislocation climb normally requires more energy and is associated with a slower rate than dislocation glide in most of the alloys, and was hence considered as the rate-controlling factor for creep [18,57].

Among the possible aforementioned deformation mechanisms which accelerate the creep rate and may strongly contribute to the creep deformation, necking instability is generally observed. In the power-law equation, the creep strain is considered to be homogeneous along the specimen axis, which is not entirely true. The creep curves obtained are, thus, a combination of the operating creep mechanisms in the material and the development of a neck. Indeed, the local deformation behaviour is expected to be creep influenced in the regions away from the necked region. However, at the regions near to the rupture surface, the behaviour is mainly plasticity driven. This can be consolidated by an FE analysis conducted on MarBN steel using a Benchmark neck-based model under creep conditions (Fig. 16). It can be seen from the FE results that, at the necked region (Region B), the equivalent plastic strain is predominantly accommodated (mostly concentrated at the rupture surface). However, at the regions away from the rupture surface (Region A), the values of the equivalent plastic strain are tenfold lower compared to those of Region B, where spatial distributions seem to be strongly heterogeneous.

Although the power-law equation is found to be in good agreement with the experimental observations, it cannot reflect the possible physical mechanisms involved during the creep process. In order to have a better understanding of the physical processes during short-term creep testing of MarBN, detailed microstructural characterisation was conducted in both the non-necked and the necked parts of gauge portion (i.e. typically 5 mm and 20 mm away from the rupture surface, respectively) to link with the characteristics of global creep behaviour as presented above. Important observations of the microstructure after short-term creep testing are summarised as follows: i) the martensitic microstructure in the non-necked part of gauge portion appears similar to the stress-free head portion, whereas the original microstructure was significantly changed in the necked part during short-term creep (Figs. 12–13), ii) a much higher extent of damage is presented in the necked part of the gauge portion than the non-necked part (Fig. 9), with a close association between damage and inclusion particles observed in both areas (Fig. 8), iii) compared to the specimen tested under a lower stress (i.e. 200 MPa), the specimen tested under a higher stress (i.e. 280 MPa) shows a lower average area of martensitic blocks and a longer normalised intercept length along the principal stress direction in both the non-necked and the necked parts of gauge portion (Fig. 13), iv) significant refinement of the martensitic lath structure was observed in the necked part of the gauge portion in both of the specimens tested at 650°C, whereas the lath structure in the specimen tested under a high stress (i.e. 280 MPa) is more refined (Fig. 15), v) dislocation interactions, such as dislocation jogs, tangles and pile-ups, and the interaction between dislocations and secondary precipitates were extensively observed within the lath interiors (Fig. 15). Fig. 17 shows schematic diagrams summarising the microstructural observations from both the stress-free head portion and the non-necked and necked parts from the gauge portion.

The different characteristics of the microstructure and damage distribution between the necked and the non-necked parts of gauge portion are attributed to the significant plastic strain presented in the necked part in addition to the creep strain accumulated in the same area before the onset of necking (Fig. 17). The distorted, refined martensitic microstructure in the necked part is evidence of plastic strain as this microstructure is similar to the cell block grain structure formed after extensive plastic deformation with a high strain rate [61–63]. The scale of the cell-block grain structure is also decreased at an increased strain intensity [62], and this is consistent with the observation of a more refined substructure presented in the specimen showing significant necking (i.e. 81.8% for the 650°C/280 MPa specimen, Table 2).

Under the influence of plastic strain, the damage presented in the necked part is formed as micro-voids elongated along the principal stress direction as a result of plastic flow in the surrounding matrix [7]. The close association between the plasticity induced micro-voids and the inclusion particles in the necked part (Fig. 8) is consistent with the previous report of plastic damage, which is preferentially formed on secondary phase particles [6,7]. However, one should also bear in mind that the micro-voids might be formed via a more complex scenario by transforming from the ‘pre-existing’ creep damage formed before the onset of necking. This is supported by the observation that damage was also formed on inclusion particles in the non-necked part of gauge portions (Fig. 8) (i.e. similar to the previous reports from other 9% Cr steels [52,64,65]).

It can be inferred from the aforementioned observations that both dislocation climb-controlled creep and plastic instability (necking development) can occur, interact and strongly contribute to the macroscopic degradation of the material at high stress regimes and elevated temperatures. Note that other “secondary” creep mechanisms such as grain boundary sliding and/or lattice diffusion, may be active, even with small contributions, and can play an important role in the short-term creep deformation of MarBN steel. The theoretical computations and microstructural observations have been combined to better elucidate and emphasize the dominant deformation mechanisms. Although literature is abundant of empirical equations for the power-law regime, there is still a need to understand and thus track most of the physical mechanisms occurring during the creep deformation process. The demand for an accurate and reliable modelling framework that accounts for the microstructural evolution is of prime importance to gain further insight into the deformation mechanisms of MarBN steel. Models based on dislocation density should have a stronger physical meaning. Dislocation densities can thus be incorporated as internal state variables, and their evolution can be modelled based on the storage and annihilation processes for dislocations.

5. Conclusions

An extensive experimental investigation has been conducted to understand the short-term creep behaviour of MarBN steel at high temperature. The experimental study combines macroscopic predictions (through empirical formulations) and microstructural evidence (through SEM, EBSD and TEM investigations). The main objectives of the experimental work were to *1)* investigate the possible relationships that may exist between the creep strain rate and internal variables, *2)* decouple both creep and local plasticity-driven mechanisms, and *3)* emphasize the true rate-controlling creep mechanism in the MarBN steel at the selected temperatures and stress levels. The findings obtained are thus summarised as follows:

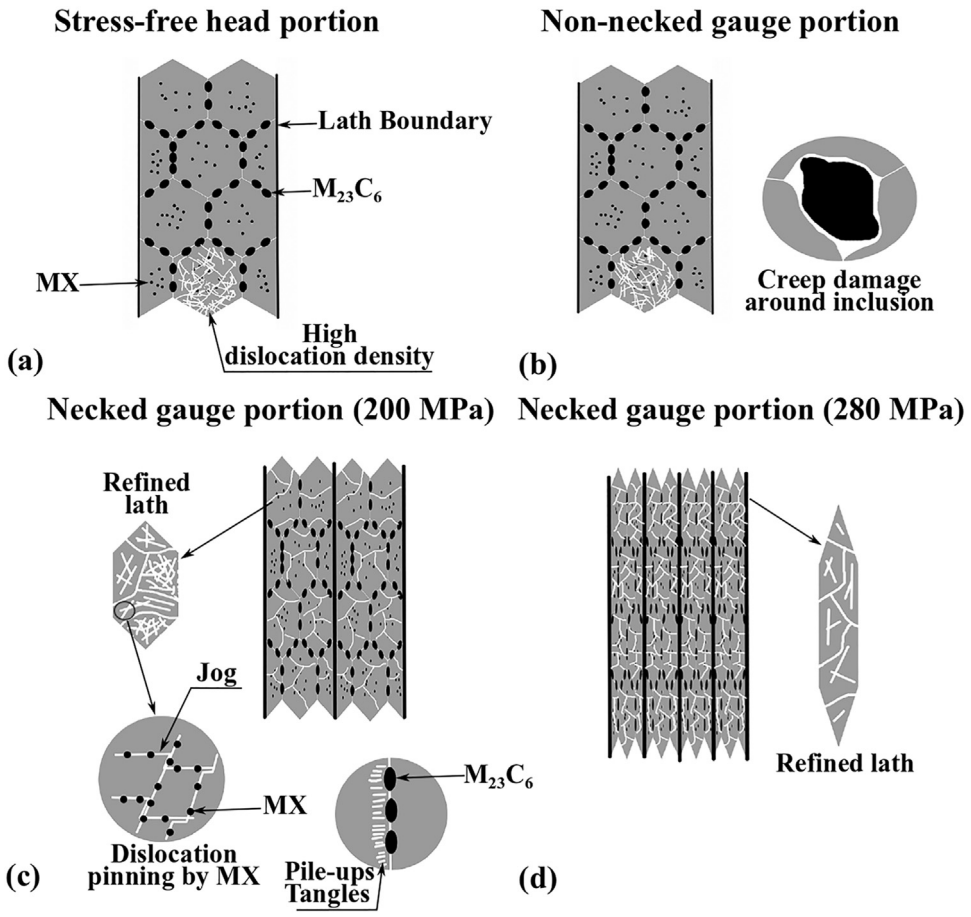

Fig. 17. Schematic diagrams illustrating the microstructural states in (a) the stress-free head portion, (b) the non-necked part in gauge portion, the necked part in the gauge portion after creep tests at an applied stress of (c) 200 MPa and (d) 280 MPa.

1. The steady-state creep of MarBN steel obeys the power and Arrhenius laws as well as the modified Monkman-Grant empirical formulae. High values of apparent stress exponents and activation energies have been obtained.
2. A power-law stress dependence with an exponent of 7 (SSCR $\propto\sigma^7$) has been obtained. The corresponding real activation energy was about 307.82 kJ mol^{-1}, which is found to be close to the lattice self-diffusion energy in Cr. These values suggest that climb-controlled creep is likely to be the dominating rate-controlling mechanism in MarBN steel at high temperature and high stresses.
3. Necking instability was also observed in the failed specimens, highlighting the local plasticity at the necked region. Micro-voids were nucleated on inclusions and tend to elongate near the rupture surface due to the high plasticity. Grain refinement and distortion of the grain structure under plastic flow has also been observed. An inhomogeneous dislocation structure including jogs, tangles and pile-ups has been demonstrated near the rupture surface.

Note that the power law is very flexible and can easily change expressions by adding the aforementioned internal variables, hence the real stress exponent and real activation energy can be re-evaluated to better emphasize the rate-controlled creep mechanism. By analysing the foregoing results, most of the mechanisms governing the creep behaviour of the MarBN steel have been highlighted. Both dislocation climb-controlled creep and plastic instability (necking development) can occur, interact and strongly contribute to the macroscopic degradation of the material at high stress regimes and elevated temperatures.

Acknowledgments

This work was supported by the Engineering and Physical Sciences Research Council [grant numbers EP/N509991/1, EP/N509942/1].

The authors gratefully acknowledge the following partners for their valuable contributions: Doosan Babcock, GE Power, Uniper Technologies, Metrode Products, Goodwin Steel Castings and Wyman-Gordon. Specific acknowledgments to M. Bartosz Polomski (GE Power) for providing the test material and M. Shane Maskill (University of Nottingham) for his support in the experimental testing. The authors also acknowledge use of facilities within the Loughborough Materials Characterisation Centre.

The authors would also like to warmly thank Dr. Martin Strangwood (University of Birmingham) for fruitful discussions about the microstructure analysis and complementary suggestions.

References

[1] B. Fournier, F. Dalle, M. Sauzay, J. Longour, M. Salvi, C. Caës, I. Tournié, P.F. Giroux, S.H. Kim, Comparison of various 9-12%Cr steels under fatigue and creep-fatigue loadings at high temperature, Mater. Sci. Eng. A 528 (2011) 6934–6945, https://doi.org/10.1016/j.msea.2011.05.046.

[2] D.J. Benac, H.S. Reemsnyder, Failure analysis and life assessment of structural components and equipment, ASM Int. Handb. Fail. Anal. Prev. 11 (2002) 184, https://doi.org/10.1361/asmhba0003512.

[3] F. Abe, M. Tabuchi, H. Semba, M. Igarashi, M. Yoshizawa, N. Komar, A. Fujita, Feasibility of MARBN steel for application to thick section boiler components in USC power plant at 650°C, in: Adv. Mater. Technol. Foss. Power Plants - from in: Proceedings of the 5th International Conference: 2008: pp. 92–106. <https://doi.org/10.1361/cp2007epri0092>.

[4] E.N. da, C. Andrade, On the Viscous Flow in Metals, and Allied Phenomena, Proc. R. Soc. A Math. Phys. Eng. Sci 84 (1910), pp. 1–12, https://doi.org/10.1098/rspa.1910.0050.

[5] F.R.N. Nabarro, H.L. Villiers, The Physics of Creep 17 Elsevier Sci, 1995, p. 413, https://doi.org/10.1016/0966-9795(96)00037-4.
[6] M.E. Kassner, T.A. Hayes, Creep cavitation in metals, Int. J. Plast. 19 (2003) 1715–1748.
[7] J. Lin, Y. Liu, T.A. Dean, A review on damage mechanisms, models and calibration methods under various deformation conditions, Int. J. Damage Mech. 14 (2005) 299–319.
[8] K.T. Park, E.J. Lavernia, F.A. Mohamed, High temperature creep of silicon carbide particulate reinforced aluminum, Acta Metall. Mater. 38 (1990) 2149–2159, https://doi.org/10.1016/0956-7151(90)90082-R.
[9] F.C. Monkman, N.J. Grant, An empirical relationship between rupture life and minimum creep rate in creep-rupture tests, Proc. ASTM, 1956, pp. 593–620.
[10] V.M. Radhakrishnan, The relationship between minimum creep rate and rupture time in Cr-Mo steels, J. Mater. Eng. Perform. 1 (1992) 123–128, https://doi.org/10.1007/BF02650043.
[11] G. Dimmler, P. Weinert, H. Cerjak, Extrapolation of short-term creep rupture data-The potential risk of over-estimation, Int. J. Press. Vessel. Pip. 85 (2008) 55–62, https://doi.org/10.1016/j.ijpvp.2007.06.003.
[12] B. Wilshire, P.J. Scharning, Extrapolation of creep life data for 1Cr-0.5Mo steel, Int. J. Press. Vessel. Pip. 85 (2008) 739–743, https://doi.org/10.1016/j.ijpvp.2008.04.002.
[13] M.F. Ashby, A first report on deformation-mechanism maps, Acta Metall. 20 (1972) 887–897, https://doi.org/10.1016/0001-6160(72)90082-X.
[14] M.F. Ashby, H.J. Frost, Deformation-mechanism Maps, Oxford Pergamon Press, 1982, pp. 44–45.
[15] J.P. Poirier, Creep of Crystals, Cambridge University Press, 1985.
[16] O.D. Sherby, A.K. Miller, Combining phenomenology and physics in describing the high temperature mechanical behavior of crystalline solids, J. Eng. Mater. Technol. 101 (1979) 387–395, https://doi.org/10.1115/1.3443708.
[17] R.L. Coble, A model for boundary diffusion controlled creep in polycrystalline materials, J. Appl. Phys. 34 (1963) 1679–1682, https://doi.org/10.1063/1.1702656.
[18] P.M. Burke, O.D. Sherby, Mechanical behavior of crystalline solids at elevated temperature, Prog. Mater. Sci. 13 (1968) 323–390.
[19] P.J. Ennis, A. Czyrska-Filemonowicz, Recent advances in creep-resistant steels for power plant applications, Sadhana 28 (2003) 709–730.
[20] K. Maruyama, K. Sawada, J. Koike, Strengthening mechanisms of creep resistant tempered martensitic steel, ISIJ Int. 41 (2001) 641–653.
[21] J. Pešička, R. Kužel, A. Dronhofer, G. Eggeler, The evolution of dislocation density during heat treatment and creep of tempered martensite ferritic steels, Acta Mater. 51 (2003) 4847–4862, https://doi.org/10.1016/S1359-6454(03)00324-0.
[22] C.G. Panait, A. Zielińska-Lipiec, T. Koziel, A. Czyrska-Filemonowicz, A.-F. Gourgues-Lorenzon, W. Bendick, Evolution of dislocation density, size of subgrains and MX-type precipitates in a P91 steel during creep and during thermal ageing at 600 °C for more than 100,000 h, Mater. Sci. Eng. A 527 (2010) 4062–4069.
[23] M. Mitsuhara, S. Yamasaki, M. Miake, H. Nakashima, M. Nishida, J. Kusumoto, A. Kanaya, Creep strengthening by lath boundaries in 9Cr ferritic heat-resistant steel, Philos. Mag. Lett. 96 (2016) 76–83, https://doi.org/10.1080/09500839.2016.1154200.
[24] W. Yan, W. Wang, Y.-Y. Shan, K. Yang, Microstructural stability of 9–12% Cr ferrite/martensite heat-resistant steels, Front. Mater. Sci. 7 (2013) 1–27.
[25] P.-F. Giroux, F. Dalle, M. Sauzay, J. Malaplate, B. Fournier, A.-F. Gourgues-Lorenzon, Mechanical and microstructural stability of P92 steel under uniaxial tension at high temperature, Mater. Sci. Eng. A 527 (2010) 3984–3993.
[26] B. Xiao, L. Xu, L. Zhao, H. Jing, Y. Han, Z. Tang, Microstructure evolution and fracture mechanism of a novel 9Cr tempered martensite ferritic steel during short-term creep, Mater. Sci. Eng. A 707 (2017) 466–477, https://doi.org/10.1016/j.msea.2017.09.086.
[27] E. Cerri, E. Evangelista, S. Spigarelli, P. Bianchi, Evolution of microstructure in a modified 9Cr–1Mo steel during short term creep, Mater. Sci. Eng. A 245 (1998) 285–292, https://doi.org/10.1016/S0921-5093(97)00717-X.
[28] F. ABe, Effect of fine precipitation and subsequent coarsening of Fe2W Laves phase on the creep deformation behavior of tempered martensitic 9Cr-W steels, Metall. Mater. Trans. A. 36 (2005) 321–332.
[29] G. Eggeler, The effect of long-term creep on particle coarsening in tempered martensite ferritic steels, Acta Metall. 37 (1989) 3225–3234.
[30] J. Hald, L. Korcakova, Precipitate stability in creep resistant ferritic steels-experimental investigations and modelling, ISIJ Int. 43 (2003) 420–427, https://doi.org/10.2355/isijinternational.43.420.
[31] F. Abe, Precipitate design for creep strengthening of 9% Cr tempered martensitic steel for ultra-supercritical power plants, Sci. Technol. Adv. Mater. 9 (2008) 13002.
[32] L. Maddi, D. Barbadikar, M. Sahare, A.R. Ballal, D.R. Peshwe, R.K. Paretkar, K. Laha, M.D. Mathew, Microstructure evolution during short term creep of 9Cr–0.5Mo–1.8W steel, Trans. Indian Inst. Met. 68 (2015) 259–266, https://doi.org/10.1007/s12666-015-0586-9.
[33] T. Shrestha, M. Basirat, I. Charit, G.P. Potirniche, K.K. Rink, Creep rupture behavior of Grade 91 steel, Mater. Sci. Eng. A 565 (2013) 382–391, https://doi.org/10.1016/j.msea.2012.12.031.
[34] L.A. Giannuzzi, B.W. Kempshall, S.M. Schwarz, J.K. Lomness, B.I. Prenitzer, F.A. Stevie, F.I.B. Lift-Out, Specimen preparation techniques, in: L.A. Giannuzzi, F.A. Stevie (Eds.), Introd. to Focus. Ion Beams Instrumentation, Theory, Tech. Pract. Springer US, Boston, MA, 2005, pp. 201–228, , https://doi.org/10.1007/0-387-23313-X_10.
[35] D.R. Jara, 9-12 % Cr Heat Resistant Steels : Alloy Design, TEM Characterisation of Microstructure Evolution and Creep Response at 650 °C, (2011).
[36] J. Pe??i??ka, A. Aghajani, C. Somsen, A. Hartmaier, G. Eggeler, How dislocation substructures evolve during long-term creep of a 12% Cr tempered martensitic ferritic steel, Scr. Mater. 62 (2010) 353–356, https://doi.org/10.1016/j.scriptamat.2009.10.037.
[37] D.C. Dunand, B.Q. Han, a.M. Jansen, Monkman-grant analysis of creep fracture in dispersion-strengthened and particulate-reinforced aluminum, Metall. Mater. Trans. A 30 (1999) 829–838, https://doi.org/10.1007/s11661-999-1016-6.
[38] H. Ghassemi Armaki, K. Maruyama, M. Yoshizawa, M. Igarashi, Prevention of the overestimation of long-term creep rupture life by multiregion analysis in strength enhanced high Cr ferritic steels, Mater. Sci. Eng. A 490 (2008) 66–71, https://doi.org/10.1016/j.msea.2008.01.072.
[39] L. Kloc, V. Sklenička, Transition from power-law to viscous creep behaviour of p-91 type heat-resistant steel, Mater. Sci. Eng. A 234–236 (1997) 962–965, https://doi.org/10.1016/S0921-5093(97)00364-X.
[40] B.K. Choudhary, E. Isaac Samuel, Creep behaviour of modified 9Cr-1Mo ferritic steel, J. Nucl. Mater. 412 (2011) 82–89, https://doi.org/10.1016/j.jnucmat.2011.02.024.
[41] R.S. Mishra, A.B. Pandey, Some observations on the high-temperature creep behavior of 6061 Al-SiC composites, Metall. Trans. A 21 (1990) 2089–2090, https://doi.org/10.1007/BF02647258.
[42] J.R. Cahoon, O.D. Sherby, Activation energy for lattice self-diffusion and the Engel-Brewer theory, Metall. Trans. A Phys. Metall. Mater. Sci. 23 (1992) 2491–2500.
[43] J. Onoro, Martensite microstructure of 9–12% Cr steels weld metals, J. Mater. Process. Technol. 180 (2006) 137–142.
[44] L. Ryde, Application of EBSD to analysis of microstructures in commercial steels, Mater. Sci. Technol. 22 (2006) 1297–1306.
[45] H. Kitahara, R. Ueji, N. Tsuji, Y. Minamino, Crystallographic features of lath martensite in low-carbon steel, Acta Mater. 54 (2006) 1279–1288.
[46] T. Hamaguchi, H. Okada, S. Kurihara, H. Hirata, M. Yoshizawa, A. Iseda, Microstructural Evaluation of 9Cr-3W-3Co-Nd-B Heat-Resistant Steel (SAVE12AD) After Long-Term Creep Deformation, V06AT06A064, (2017). 〈http://dx.doi.org/10.1115/PVP2017-65241〉.
[47] A. Chauhan, D. Litvinov, Y. de Carlan, J. Aktaa, Study of the deformation and damage mechanisms of a 9Cr-ODS steel: microstructure evolution and fracture characteristics, Mater. Sci. Eng. A 658 (2016) 123–134.
[48] D. Richardot, J.C. Vaillant, A. Arbab, W. Bendick, The T92/P92 book Vallourec-Mannesmann Tubes, (2000).
[49] P. Polcik, T. Sailer, W. Blum, S. Straub, J. Buršík, A. Orlová, On the microstructural development of the tempered martensitic Cr-steel P 91 during long-term creep—a comparison of data, Mater. Sci. Eng. A 260 (1999) 252–259, https://doi.org/10.1016/S0921-5093(98)00887-9.
[50] A. Orlová, J. Čadek, Dislocation structure in the high temperature creep of metals and solid solution alloys: a review, Mater. Sci. Eng. 77 (1986) 1–18.
[51] P.Z.L. Li, G. West, R.C. Thomson, The Effect of Stress Relief Heat Treatments on Microstructural Evolution and Mechanical Properties in Grade 91 and 92 Power Plant Steels, (2011), pp. 679–692.
[52] Y. Gu, G.D. West, R.C. Thomson, J. Parker, Investigation of Creep Damage and Cavitation Mechanisms in P92 Steels, (2014).
[53] X. Xu, G.D. West, J.A. Siefert, J.D. Parker, R.C. Thomson, Microstructural characterization of the heat-affected zones in Grade 92 steel welds: double-pass and multipass welds, Metall. Mater. Trans. A 49 (2018) 1211–1230, https://doi.org/10.1007/s11661-017-4446-6.
[54] J. Hald, Microstructure and long-term creep properties of 9–12% Cr steels, Int. J. Press. Vessel. Pip. 85 (2008) 30–37.
[55] F. Abe, M. Taneike, K. Sawada, Alloy design of creep resistant 9Cr steel using a dispersion of nano-sized carbonitrides, Int. J. Press. Vessel. Pip. 84 (2007) 3–12.
[56] H. Semba, F. Abe, Alloy design and creep strength of advanced 9%Cr USC boiler steels containing high concentration of boron, Energy Mater. 1 (2006) 238–244, https://doi.org/10.1179/174892406×173611.
[57] J.E. Dorn, Some fundamental experiments on high temperature creep, J. Mech. Phys. Solids 3 (1955) 85–116, https://doi.org/10.1016/0022-5096(55)90054-5.
[58] L. Falat, A. Výrostková, V. Homolová, M. Svoboda, Creep deformation and failure of E911/E911 and P92/P92 similar weld-joints, Eng. Fail. Anal. 16 (2009) 2114–2120.
[59] T. Shrestha, M. Basirat, S. Alsagabi, A. Sittiho, I. Charit, G.P. Potirniche, Creep rupture behavior of welded Grade 91 steel, Mater. Sci. Eng. A 669 (2016) 75–86, https://doi.org/10.1016/j.msea.2016.05.065.
[60] D. Hull, D.J. Bacon, Introduction to Dislocations, Elsevier, 2011.
[61] Z.B. Zhang, O.V. Mishin, N.R. Tao, W. Pantleon, Microstructure and annealing behavior of a modified 9Cr − 1Mo steel after dynamic plastic deformation to different strains, J. Nucl. Mater. 458 (2015) 64–69, https://doi.org/10.1016/j.jnucmat.2014.12.001.
[62] X. Huang, S. Morito, N. Hansen, T. Maki, Ultrafine structure and high strength in cold-rolled martensite, Metall. Mater. Trans. A 43 (2012) 3517–3531, https://doi.org/10.1007/s11661-012-1275-5.
[63] C.Y. Barlow, N. Hansen, Y.L. Liu, Fine scale structures from deformation of aluminium containing small alumina particles, Acta Mater. 50 (2002) 171–182, https://doi.org/10.1016/S1359-6454(01)00330-5.
[64] K. Sakuraya, H. Okada, F. Abe, BN type inclusions formed in high Cr ferritic heat resistant steel, Energy Mater. (2013).
[65] K. Sakuraya, H. Okada, F. Abe, Influence of heat treatment on formation behavior of boron nitride inclusions in P122 heat resistant steel, ISIJ Int. 46 (2006) 1712–1719.
[66] S. Spigarelli, Constitutive equations in creep of Mg-Al alloys, Mater. Sci. Eng. A 492 (2008) 153–160, https://doi.org/10.1016/j.msea.2008.03.007.
[67] T. Shrestha, M. Basirat, I. Charit, G.P. Potirniche, K.K. Rink, U. Sahaym, Creep deformation mechanisms in modified 9Cr-1Mo steel, J. Nucl. Mater. 423 (2012) 110–119, https://doi.org/10.1016/j.jnucmat.2012.01.005.
[68] O.D. Sherby, R.H. Klundt, A.K. Miller, Flow stress, subgrain size, and subgrain stability at elevated temperature, Metall. Trans. A 8 (1977) 843–850, https://doi.org/10.1007/BF02661565.